On-the-fly motion-compensated cone-beam CT using an *a priori* model of the respiratory motion

Simon Rit, Jochem W. H. Wolthaus, Marcel van Herk, and Jan-Jakob Sonke[a)]
Department of Radiation Oncology, The Netherlands Cancer Institute-Antoni van Leeuwenhoek Hospital, Plesmanlaan 121, 1066 CX Amsterdam, The Netherlands

(Received 14 November 2008; revised 17 March 2009; accepted for publication 17 March 2009; published 27 May 2009)

Respiratory motion causes artifacts in cone-beam (CB) CT images acquired on slow rotating scanners integrated with linear accelerators. Respiration-correlated CBCT has been proposed to correct for the respiratory motion but only a subset of the CB projections is used to reconstruct each frame of the 4D CBCT image and, therefore, adequate image quality requires long acquisition times. In this article, the authors develop an on-the-fly solution to estimate and compensate for the respiratory motion in the reconstruction of a 3D CBCT image from all the CB projections. An *a priori* motion model of the patient respiratory cycle is estimated from the 4D planning CT. During the acquisition, the model is correlated with the respiration using a respiratory signal extracted from the CB projections. The estimated motion is next compensated for in an optimized reconstruction algorithm. The motion compensated for is forced to be null on average over the acquisition time to ensure that the compensation results in a CBCT image which describes the mean position of each organ, even if the *a priori* motion model is inaccurate. Results were assessed on simulated, phantom, and patient data. In all experiments, blur was visually reduced by motion-compensated CBCT. Simulations showed robustness to inaccuracies of the motion model observed on patient data such as amplitude variations, phase shifts, and setup errors, thus proving the efficiency of the compensation using an *a priori* motion model. Noise and view-aliasing artifacts were lower on motion-compensated CBCT images with 1 min scan than on respiration-correlated CBCT images with 4 min scan. Finally, on-the-fly motion estimation and motion-compensated reconstruction were within the acquisition time of the CB projections and the CBCT image available a few seconds after the end of the acquisition. In conclusion, the authors developed and implemented a method for correcting the respiratory motion during the treatment fractions which can replace respiration-correlated CBCT for improving image quality while decreasing acquisition time. © *2009 American Association of Physicists in Medicine*. [DOI: 10.1118/1.3115691]

Key words: motion compensation, image guided radiation therapy, cone-beam CT, organ motion, reconstruction

I. INTRODUCTION

Recently, cone-beam (CB) computed tomography (CT) scanners have been integrated with linear accelerators to acquire three dimensional (3D) CBCT images of the patients for image guidance of radiotherapy.[1] These 3D CBCT images allow to correct for the target misalignment and adapt the treatment plan.[2] However, respiratory motion causes artifacts in CBCT images of the thoracic and upper abdominal region, such as blur and streaks, which are known to reduce the accuracy of derived information.[3]

A first solution to account for the respiratory motion is respiration-correlated CBCT.[4–7] It consists of sorting the CB projections depending on their position in the respiratory cycle assessed with a respiratory signal. Each subset of CB projections is then used to reconstruct a 3D CBCT image (or frame) representing one phase of the respiratory cycle, thus obtaining a 4D CBCT image of the respiratory cycle. A 4D CBCT approach has been successfully implemented in our institution for guidance of lung cancer radiotherapy.[8] However, the insufficient angular sampling of the CB projections per respiratory phase causes view-aliasing artifacts characterized by high-frequency streaks. These artifacts can be reduced by slowing down the gantry[7] or doing multiple rotations[6] but it substantially lengthens the fraction duration. Moreover, acquisition times that are clinically acceptable do not offer adequate image quality for guidance of upper abdominal lesions.

An alternative solution is motion-compensated CBCT.[9] The method is two step: first, it estimates the patient motion during the CB acquisition and second, it uses the estimated motion in the reconstruction algorithm. Thus, a 3D CBCT image at a reference position is reconstructed from all the CB projections. It has been shown on simulated data that this method can correct for the respiratory motion without view-aliasing artifacts.[9] Nevertheless, estimating the motion on real CB projections is still a challenge. Several solutions have been proposed[10,11] but their computational cost added to the cost of the reconstruction algorithm has prevented the clinical use of motion-compensated CBCT.

In this paper, we develop an on-the-fly solution for motion-compensated CBCT, i.e. motion estimation and its compensation in the reconstruction during the acquisition of

TABLE I. Characteristics of the data sets used in this work.

Study	Gantry speed	Number of CB projections	X-ray tube parameters
Simulation without motion	Slow	1300	
Simulation with motion	Slow		–
Phantom without motion	Fast	387	16 mA/40 ms
Phantom with motion	Slow	1353	16 mA/20 ms
	Fast	375	16 mA/40 ms
Lung patient	Slow	1392	16 mA/40 ms
	Fast	361	16 mA/40 ms
Liver patient	Slow	1320	32 mA/40 ms
	Fast	221	32 mA/40 ms

the CB projections. Motion estimation uses an *a priori* model of the patient motion over a respiratory cycle estimated from the 4D CT image acquired on a conventional CT scanner for treatment planning. During the acquisition, the model is correlated with the respiration using a respiratory signal extracted from the CB projections. The estimated motion is next compensated for in an optimized reconstruction algorithm. Speed, robustness, and image quality were evaluated on simulated data and on real data of a mechanical phantom. Proof of the concept was demonstrated on two patients, a lung cancer patient and a liver cancer patient.

II. MATERIALS AND METHODS

II.A. CT scanners

II.A.1. Planning CT

Planning CT images were acquired on a helical CT scanner (24-slice Somatom Sensation Open, Siemens, Forchheim, Germany) synchronized with the respiration using a thermometer at the entry of a nasobuccal oxygen mask (see Ref. 12 for more details on the protocol). 4D CT images were reconstructed with $F=10$ frames equally distributed in time and a $1\times1\times3$ mm^3 voxel resolution.

II.A.2. Cone-beam CT

Cone-beam projections were acquired on a linear accelerator with kV imaging capability (Synergy, Elekta Oncology Systems, Crawley, UK). The source-to-isocenter distance was 100 cm and the source-to-panel distance was 154 cm. The flat panel provided 41×41 cm^2 projections stored at 512×512 pixel resolution, acquired at a 5.5 fps frequency using 120 kVp. A short scan (200°) was used with two different speed, 200°/min (fast) and 50°/min (slow). The other acquisition parameters are summarized in Table I. Three CBCT images were reconstructed for each sequence of CB projections: non-corrected, respiration-correlated, and motion-compensated. The resolution of reconstructed CBCT images was $256\times256\times256$ voxels of $1\times1\times1$ mm^3. Only the end-exhale frame of the respiration-correlated 4D CBCT image was evaluated in the following.

II.B. *A priori* motion model of the respiratory cycle

A model of the patient motion over the respiratory cycle was estimated *a priori* from the 4D planning CT. A phase-based optical flow method[13] adapted for thoracic CT images[14] was used to estimate the 3D deformation vector fields (DVFs) from the end-exhale frame to the other frames of the 4D CT following the procedure described in Ref. 14. We thus obtained a 4D DVF which represents the piecewise linear motion Φ over the respiratory cycle of each voxel of the 4D planning CT image [Fig. 1(a)]:

$$\Phi:\ \mathbb{R}^3\times[0;F)\rightarrow\mathbb{R}^3,$$

$$(\boldsymbol{x},p)\qquad\rightarrow\Phi(\boldsymbol{x},p)=\Phi_p(\boldsymbol{x}),\tag{1}$$

where $\boldsymbol{x}$ is the 3D vector of the spatial coordinates and p is a continuous variable representing the so-called phase of the respiratory cycle with integer values of p corresponding to the pth frame of the 4D planning CT. Linear interpolation was used to interpolate the four dimensions of the 4D DVF.

The robustness of the method to inaccuracies of the *a priori* model due to artifacts of the 4D planning CT (Ref. 15) or misregistration[16] was not specifically investigated in this study as they can be regarded as non-reproducibility of the *a priori* model. An evaluation of the registration accuracy can be found in Ref. 14. The effect of non-reproducibility of the

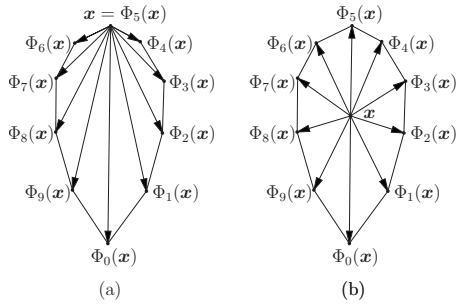

FIG. 1. 2D illustration of the trajectory of one voxel over the ten frames of the 4D planning CT image with (a) the fifth frame as a reference and (b) the mean position as a reference.

motion model on the final result was evaluated in this study using simulations (Sec. II E 1).

In our method, the reference space of the 4D DVF, which is schematically represented by the tail of the vectors, determines which position in the respiratory cycle is reconstructed. Keeping the 4D DVF as estimated would reconstruct the end-exhale position [Fig. 1(a)]. Any other position can be reconstructed so we chose the temporal mean position [Fig. 1(b)] which is the targeted position.[12] The 4D DVF respects then the following property:

$$\sum_{p=0}^{F-1} \Phi_p(\boldsymbol{x}) = \boldsymbol{x}, \quad \forall\, x \in \mathbb{R}^3. \tag{2}$$

II.C. On-the-fly motion estimation

An efficient estimation of the patient's respiratory motion during the acquisition of the CB projections was developed based on the patient's motion model of the respiratory cycle (Sec. II B). We assumed that the motion over all the respiratory cycles during the acquisition of the CB projections is identical to the motion Φ described by the 4D planning CT of the patient. Two observations support this assumption. First, a previous study showed that the mean tumor trajectory measured from 4D CBCT images reconstructed from slow scans was highly stable from fraction to fraction in a large set of patients.[17] Second, the physiologic motion of the respiratory muscles is fairly simple[18] which ensures smoothness of the respiratory motion in the thoracic and upper abdominal region except at the pleural boundary.[19] Smoothness limits inaccuracies induced by small interfraction tissue shifts both for global setup errors and local baseline shifts. Baseline shifts are variations of the time-averaged tumor position relative to the bony anatomy which have shown to be substantially larger than tumor trajectory changes.[17]

Based on this assumption, only the 4D position $(\boldsymbol{x},p)$ in the motion model [Eq. (1)] remains to be computed for each voxel of the reconstructed volume at each acquisition time of a CB projection. The spatial position $\boldsymbol{x}$ in the 4D planning CT of each voxel of the CBCT image was obtained using the rigid transformation between the planning CT and the CBCT scanners, as defined during the treatment planning. The setup error was therefore ignored for on-the-fly motion estimation. The effect of the latter simplification was evaluated using simulations (Sec. II E 1).

The respiratory phase p at each acquisition time of a CB projection was computed from the respiratory signal extracted from the CB projections as previously implemented for on-the-fly respiration-correlated CBCT.[8] Each 2D CB projection is processed with a derivative filter in the cranio-caudal direction to enhance the diaphragm and projected on the cranio-caudal axis in a 1D image. The concatenation of these 1D images for a few CB projections (>1 respiratory cycle) gives a 2D image called the "Amsterdam shroud" from which the respiratory signal is extracted with a linear correlation of adjacent columns.[20] The phase of the respiration was then computed by fitting a line for each respiratory cycle on the phase of the Hilbert transform of the respiratory signal. The phase is therefore defined in this study as linear in time per respiratory cycle, as proposed in Refs. 21 and 22.

Planning CT and CBCT acquisitions were correlated with the respiration using different respiratory signals and a mapping between the two signals was required. As the respiratory signal of the CBCT acquisition focus on the cranio-caudal motion of anatomical structures, the corresponding signal value $s(p)$ of each frame of the planning CT was set as the average in the cranio-caudal direction of the corresponding frame of the 4D DVF:

$$s(p) = \boldsymbol{u}_{\mathrm{cc}} \cdot \int_{\mathbb{R}^3} \Phi_p(\boldsymbol{x}) d\boldsymbol{x}, \tag{3}$$

where $\cdot$ denotes the scalar product and $\boldsymbol{u}_{\mathrm{cc}}$ denotes the unitary vector of the cranio-caudal axis. The phase of $s(p)$ was then computed as for the respiratory signal extracted from the CB projections, thus obtaining a linear mapping between the phase p of the motion model Φ and the phase computed from the respiratory signal extracted from the CB projections. Linearity of both the phase of the on-the-fly respiratory signal and its mapping with the phase p of the motion model guarantees that each frame of the 4D DVF is equally used over the duration of the CB acquisition to compensate for the respiratory motion. Combined with the mean position property [Eq. (2), Fig. 1(b)], it forces the estimated motion to be null on average over the acquisition time for each voxel of the reconstructed CBCT image.

The latter property is meant to prevent an inaccurate estimate of an organ position due to a change of its motion amplitude during the CB acquisition compared to the *a priori* model. Indeed, a different amplitude would lead to some residual blur around the organ. In such a case, the registration of the organ to a reference image would most likely lead to centering the organ on this blurred area. However, if the reconstructed reference position is one of the respiratory phases, the true position of the organ is not the center of the blurred area. For example, if a tumor is reconstructed at end exhale using the *a priori* motion described in Fig. 1(a) but the real motion amplitude is constant and bigger (or smaller), the motion will be undercompensated (or respectively, overcompensated) and the blurred tumor will be below (or respectively, above) its true position. On the contrary, the true position of the organ is the center of the blurred area if the reconstructed reference position is the temporal mean position [Fig. 1(b)], which is the case only when the motion compensated for is null on average over the acquisition time.

II.D. On-the-fly motion-compensated reconstruction

The reconstruction algorithm is similar to that proposed by Li *et al.*,[9] i.e. motion compensation based on the local application of the Feldkamp, Davis, and Kress (FDK) algorithm.[23] The only difference with the FDK algorithm is that the backprojection is no longer performed along the straight acquisition lines corresponding to X-rays but along the curved lines corresponding to the acquisition lines warped from the acquisition position to the mean position

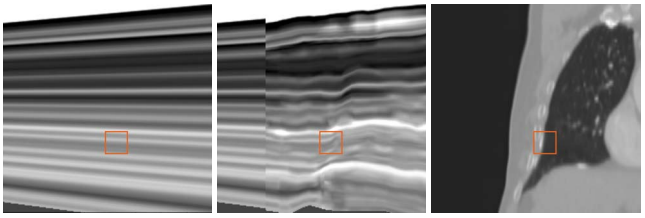

FIG. 2. Coronal slice of (a) one straight backprojection and (b) one warped backprojection. (c) Corresponding slice of the planning CT image. The drawn square corresponds to the region displayed in Fig. 3. The vertical discontinuity in (b) corresponds to the limit of the 4D DVF which is only estimated in a bounding box encompassing the patient body.

with the estimated motion (Fig. 2). Therefore, the preprocessing of the 2D CB projections was kept identical to the one of our static implementation, including correction of the ghosting effect,[24] scatter correction,[25] Parker weighting,[26] lateral padding of the data for correction of lateral truncation,[27] and Fourier ramp filtering with windowing of high frequencies.

CT reconstruction is a computationally demanding operation which has to be optimized to be achieved on the fly, i.e. within the acquisition time. Most of the computational time is spent during backprojection which has been optimized in our static implementation[28] as described in more detail in Ref. 29. In brief, the optimization uses a two-step implementation of the backprojection. First, the projection is upsampled using a bilinear interpolation (along with an alignment of the detector to the normal of the source trajectory but they are already aligned here) and it is next backprojected using a voxel-driven algorithm with a nearest neighbor interpolation. The latter step takes advantage of the detector alignment to order the nested loops so that the innermost loop has a minimal computational cost (see Fig. 2 in Ref. 29). As a consequence, the innermost loop runs along the cranio-caudal voxel segments of the CBCT image [Fig. 3(a)].

The optimization of the innermost loop relies on the preservation of the straightness with the (back)projection. As the straightness is not preserved with warped backprojections (Fig. 2), we propose to split the full-length cranio-caudal segments in l-voxel pieces [Fig. 3(b)], where l is a user parameter, and to assume that the respiratory motion preserves the straightness of these segment pieces [Fig. 3(c)]. Splitting the cranio-caudal segments allows us to run an innermost loop along each segment piece which is nearly as optimized as in the static case.

Even so, initializing the optimized innermost loop for each segment piece has a significant computational cost as its two extremities have to be successively displaced according to the respiratory motion and projected according to the x-ray transform. To reduce this cost, the number of segments was minimized by merging n consecutive l-voxel segment pieces if their distance with a single $(n\times l)$-voxel segment was smaller than a user defined threshold. The chosen distance was the square root of the quadratic mean over the

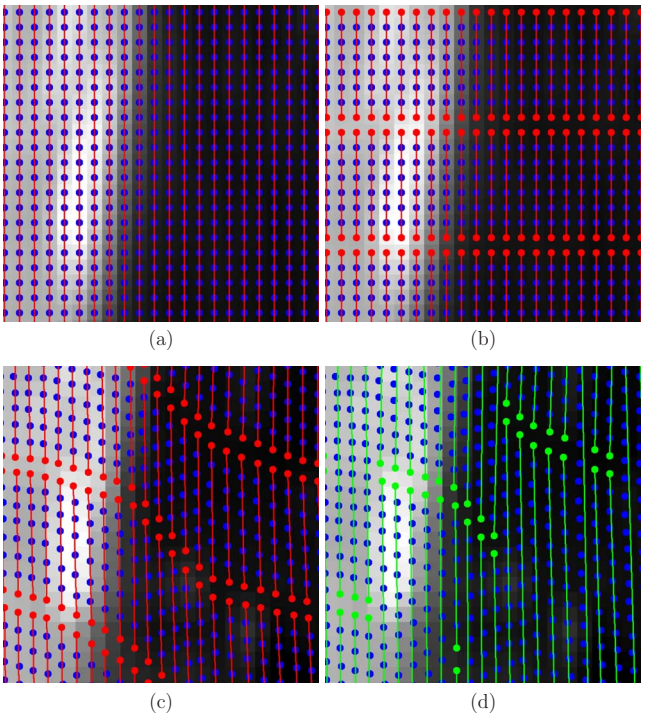

FIG. 3. 2D illustration of the voxel segments over which the optimized innermost loop of each backprojection operates. The points represent the center of the voxels. They are interconnected by a line if they belong to the same voxel segment. The background image is the region of interest drawn in Fig. 2(c). (a) Straight backprojection: the full length cranio-caudal segments are used. (b) Warped backprojection: $l=8$-voxel cranio-caudal segments are used. (c) Corresponding voxel segments after applying Φ_0 (motion from the reference to end inhale). (d) Same as in (c) with the merged voxel segments obtained using Eq. (4) with $m=0.5$ mm.

respiratory cycle of the distance between the extremities of each segment piece [Fig. 3(c)] and their corresponding position obtained by linear interpolation after merging [Fig. 3(d)]. Let us denote $[\boldsymbol{x}_{2j-1},\boldsymbol{x}_{2j}]$, $j\in\{1,\ldots,n\}$, a set of n consecutive segment pieces which belonged to the same cranio-caudal segment before splitting. Each segment $[\boldsymbol{x}_{2j-1},\boldsymbol{x}_{2j}]$ is l voxel long. Formally, the set of segments was merged to one segment $[\boldsymbol{x}_1,\boldsymbol{x}_{2n}]$ if the following criterion was respected:

$$\sqrt{\frac{1}{F}\sum_{p=0}^{F-1}\left\|\Phi_p(\boldsymbol{x}_k)-\left(\Phi_p(\boldsymbol{x}_1)+\frac{k}{2n}(\Phi_p(\boldsymbol{x}_{2n})-\Phi_p(\boldsymbol{x}_1))\right)\right\|^2}<m,$$

$$\forall k\in\{2,\ldots,2n-1\}, \tag{4}$$

where $\|\cdot\|$ is the L^2 norm and $m\in\mathbb{R}^+$ the user defined threshold.

The resulting algorithm to compute the warped backprojections can be separated into two parts. Before the CB acquisition, the segments of the reference position are initialized, which includes their selection [Eq. (4)] and warping of their coordinates with each phase of the motion model Φ_p, $\forall p\in\{0,\ldots,F-1\}$ [Fig. 3(d)]. During the acquisition, the coordinates of the segments are computed for each CB projection by linear interpolation depending on the phase value p of the signal, and the optimized loop is run over the inter-

polated segments. The latter process was multithreaded by assigning to each thread an equal number of segments to process.

II.E. Experiments

II.E.1. Simulation study

One of the main difficulties of the evaluation is that no gold standard is available for patient data. Consequently, we evaluated first the proposed method using a set of CB projections simulated from the reference CT image and the motion model of the lung patient (Sec. II E 3). The reference CT image was warped to different positions with the motion model to simulate a regular respiration with a 4 s period. Digitally reconstructed radiographies (DRRs) were then computed around the warped CT images using Joseph interpolation.[30] For comparison, the same simulation was computed without motion, i.e. without warping the reference CT image. The resulting data sets (Table I) allowed us to evaluate the following:

- Image quality and reconstruction speed depending on the user parameters l and m.
- Image quality depending on the accuracy of the motion estimation. Motion-compensated CT images were reconstructed with an altered 4D motion model Φ' to simulate:
  - phase shifts with $\Phi'_p=\Phi_{p+\Delta p}$ where $\Delta p \in [0;F)$,
  - global amplitude variations of the trajectories of the voxel with $\Phi'_p(\boldsymbol{x})=a\cdot\Phi_p(\boldsymbol{x})+(1-a)\cdot\boldsymbol{x}$ where $a\in\mathbb{R}^+$ is the amplitude variation compared to the true motion, 0% meaning no motion and 100% meaning the exact motion used for the simulation,
  - patient setup errors with $\Phi'_p=\Phi_p\circ T_R$ where T_R is a rigid transformation simulating a setup error (translations and rotations).

The results were related to the distributions of the variations of the motion model observed on two different patient data sets. The first data set contained repeat 3D CBCT images of 19 patients and was used to measure setup errors.[31] The second data set contained repeat 4D CBCT images of 56 patients and was used to measure amplitude variations and phase shifts.[17] The amplitude of each 4D CBCT was measured as the peak-to-peak amplitude of the tumor in the predominant direction of the motion. The amplitude variation was defined as the ratio between the amplitude of each 4D CBCT image with the mean amplitude over the 4D CBCT images of the same patient. The phase of each 4D CBCT was measured from the tumor motion in the predominant direction relatively to the frame number which is determined by the extracted signal that focuses on the diaphragm. The phase shift was defined as the difference between the phase of each 4D CBCT and the mean phase over the 4D CBCT images of the same patient.

Image quality of reconstructed CBCT images was quantitatively assessed with the root mean square (RMS) of the difference between the reference and the reconstructed CT images in the 128^3 mm^3 region of interest (ROI) around the isocenter (Fig. 5). The image quality is expressed in Hounsfield unit (HU).

Backprojection speed was measured on a Pentium dual-core 3.20 GHz CPU. Two threads were used for the backprojection. Backprojection speed is expressed in gigaupdate per second (GUPS) (the reconstruction of a CT image with 256^3 voxels from 256 CB projections requires four gigaupdates).

II.E.2. Phantom study

A sliced anthropomorphic static phantom of the thorax designed from a patient CT image for a previous study[32] was used in combination with a moving spherical phantom.[7] The slices of the phantom superior to the diaphragm were used. The cork representing the right lung was removed and the moving ball inserted in place. The diameter of the ball was 5 cm, the period of the motion cycle was 2.4 s, and the excursion of the ball was 8, 23, and 15 mm in the left-right (LR), superior-inferior (SI), and anterior-posterior (AP), respectively. A radio-opaque marker was placed at the center of the ball. Three sets of CB projections were acquired, one with the ball stationary (reference image) and two with the ball moving (Table I).

For easier visual comparison, respiratory-correlated and motion-compensated CBCT images were rigidly registered on the reference image. The correlation ratio assessed in a ROI encompassing the ball was used as a similarity measure. The registration result of the motion-compensated CBCT image was used for the non-corrected CBCT image.

Image quality was quantitatively assessed after registration using the signal-to-noise ratio (SNR):

$$\mathrm{SNR}\ \ (\mathrm{dB}) = 20\log_{10}\frac{\mathrm{RMS(signal)}}{\mathrm{RMS(noise)}},$$

where RMS is the root mean square of voxel intensities in the ROI, the signal is the reference image, and the noise is the voxel-to-voxel difference between the reference and the reconstructed images.

II.E.3. Patient study

Two patients with substantial respiratory motion were selected from our database to demonstrate the feasibility of the method. The first patient had a non-small cell lung cancer in the lower lobe of the right lung with a hole in the middle of the gross tumor volume (GTV). The second patient had a liver cancer with implanted radio-opaque markers around the GTV (same marker as the one used in the phantom study). The peak-to-peak amplitudes of the tumor motion measured on the 4D planning CT were 1.3 and 1.1 cm for the lung patient and the liver patient, respectively. The two patients were scanned with variable gantry rotation speeds. A fast and a slow acquisition obtained during the same treatment fraction were selected for each patient (Table I).

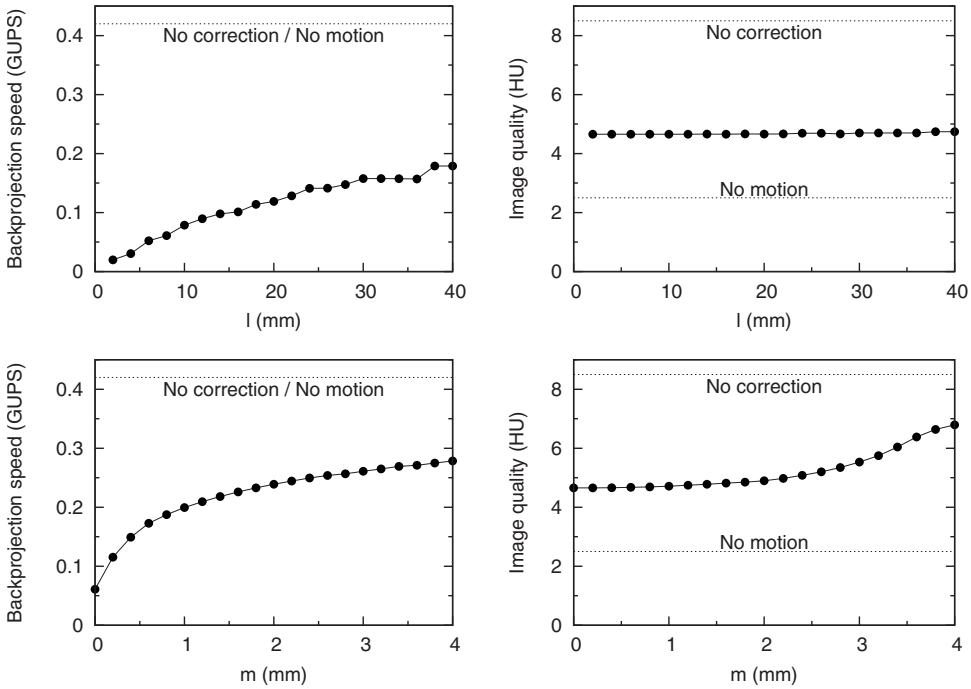

FIG. 4. Influence of the user parameters l (initial length of the segment pieces) and m (threshold for merging segment pieces) on reconstruction speed (left) and on image quality (right). First row: influence of l when $m=0$ mm. Second row: influence of m when $l=8$ mm.

The reference CT image used to evaluate the method was the mean position 3D CT image (MidP), computed from the 4D planning CT image (PI) by averaging the frames after warping them with the estimated motion Φ:

$$\mathrm{MidP}(\boldsymbol{x}) = \frac{1}{F}\sum_{p=0}^{F-1} \mathrm{PI}(\phi_p(\boldsymbol{x})), \quad \forall\, x \in \mathbb{R}^3. \tag{5}$$

Using the average instead of a particular frame allowed us to increase the signal-to-noise ratio and to blur out residual motion artifacts.[14] Although the MidP relies on the motion estimation, we have shown that the MidP represents better the anatomy of the patient than a particular frame of the 4D planning CT.[14]

Reconstructed CBCT images were spatially registered on the MidP following the procedure used for the phantom study. The ROI was the GTV for the lung patient and the liver for the liver patient, both expanded with a 5 mm margin. HUs of the CBCT images have not been calibrated on the CBCT scanner. Therefore, only relative comparison of CT numbers between MidP and CBCT images is possible. Absolute comparison of CT numbers between CBCT images of the same sequence is valid as the preprocessing of the CB projections was similar.

III. RESULTS

III.A. Simulation study

Figure 4 depicts the influence of the two user parameters l and m on the reconstruction speed and on the image quality. l is the initial length of each piece of the cranio-caudal segments of the CT images [Figs. 3(b) and 3(c)]. The backprojection speed regularly increases with l with a limited effect on the image quality. However, long segment pieces might cause the loss of details in regions where the deformation cannot be spatially approximated by a piecewise linear motion, such as the thoracic walls, so we chose a small length $l=8$ mm in the following experiments. m is the threshold in Eq. (4) below which consecutive segment pieces are merged [Fig. 3(d)]. Most of the speed improvement is obtained for small values of m because segment pieces are merged in the static parts of the image. The effect on image quality is very limited for $m<2$ mm so we chose $m=1$ mm in the rest of the study. With these values for the user parameters ($l=8$ mm and $m=1$ mm), the warped backprojection is 1.7 times slower than straight backprojection and the RMS of the error with the original image is 4.8 HU. In comparison, no approximation ($l=2$ mm and $m=0$ mm) is 21 times slower and 4.7 HU.

Figure 5 illustrates these observations visually. In the first column, the CT image obtained in the static case (reference) shows the artifacts caused by the truncation of the CB projections and by the shortness of the CB acquisitions (only 200° gantry rotation). The effect seems more limited in the chosen ROI in which the results were quantitatively assessed. In the second column, the respiratory motion implies artifacts around the thoracic walls when the motion is not corrected. In the third and fourth columns, most of the motion artifacts are eliminated when motion-compensated CBCT is used but some slight streaks remain, mainly due to the heuristic nature of the motion compensation in the reconstruction algorithm.[33] No difference is observed between the

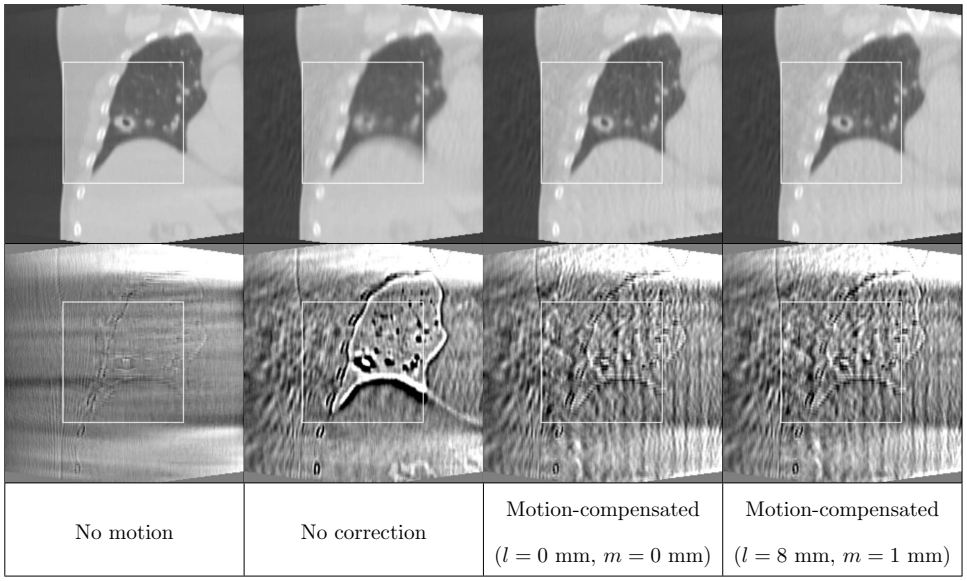

FIG. 5. First line: coronal slices of CBCT images reconstructed from the two simulated sequences of CB projections. Gray level window: [−500,1500]. Second line: difference with the corresponding slice of the reference CT image. Gray level window: [−100,100]. The white rectangle delimits the ROI which was quantitatively analyzed (Figs. 4 and 6).

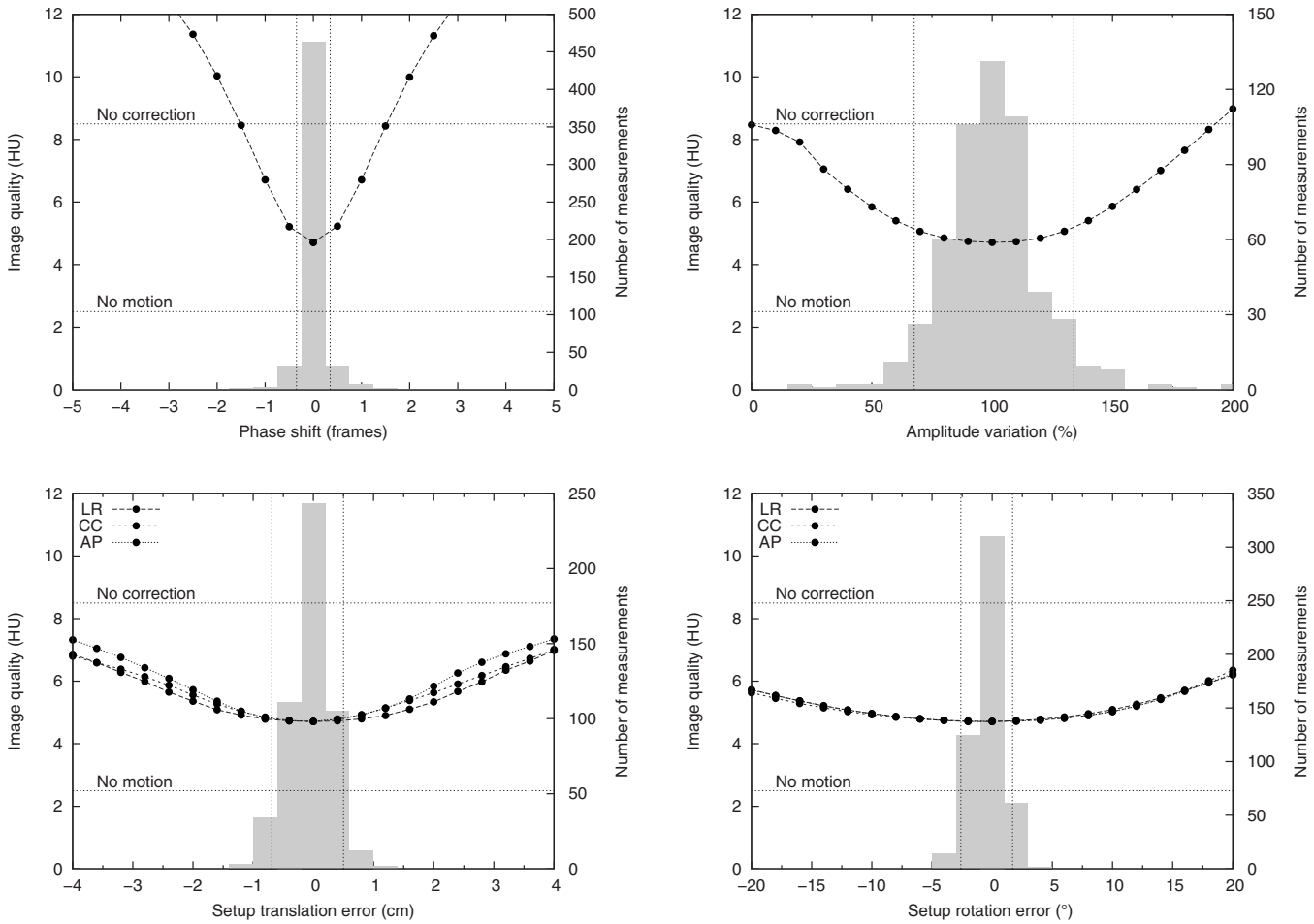

FIG. 6. Influence of various types of motion estimation errors on the image quality (left axis) superimposed on the corresponding histograms of the errors observed on patient CBCT images (right axis). Vertical dashed lines represent the 5th and the 95th percentiles. Horizontal dashed lines represent the RMS of the reconstruction error when there is no motion and when the motion is not corrected (Fig. 5).

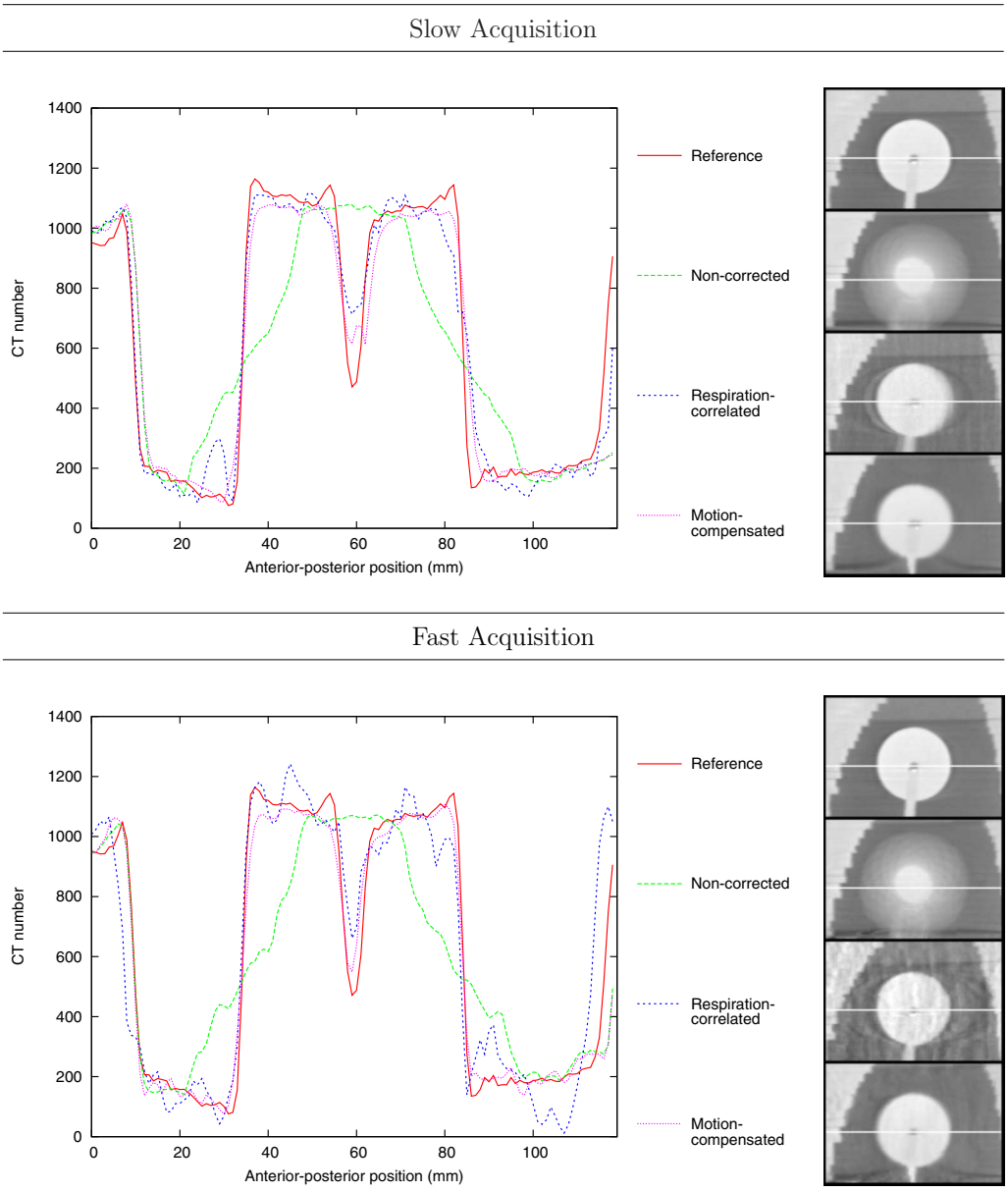

FIG. 7. Left: profiles of the CBCT images reconstructed from the slow and fast CB acquisitions of the moving mechanical phantom. Right: zooms on the coronal slices of the CT images with the white lines corresponding to the profile locations. Gray level window: [−500,1500].

exact but slow warped backprojection ($l=0$ mm and $m=0$ mm) and our approximate but faster implementation ($l=8$ mm and $m=1$ mm).

Figure 6 shows plots of the effect on image quality of various types of errors in the motion estimation, superimposed on histograms of the distribution of the corresponding errors observed on patient data. The most sensitive type of error is the phase shift. Indeed, a phase shift would drive the method to compensate for the motion in a wrong direction and, in this case, would significantly degrade the image quality for a phase shift exceeding one frame. Amplitude variations and setup errors could also alter the image quality but small variations around the ideal value have a limited effect on image quality. If the *a priori* model represents the average cycle, the effect on image quality would be limited for 90% of the population for all error types (population between the vertical lines). Note that most of the outliers in the distributions of the amplitude errors are due to measurement imprecisions when the tumor motion is very small.

III.B. Phantom study

Figure 7 provides profiles and sagittal slices of the images reconstructed from the CB acquisitions of the mechanical phantom. The non-corrected CBCT images present clear motion artifacts: the outer contour of the ball is significantly smoothed and the hole in the middle of the ball is blurred out. Respiration-correlated CBCT corrects these artifacts at the cost of statistical noise and streak artifacts due to view aliasing both in the stationary and moving parts of the phantom. The streaks are less pronounced on slow acquisition than on fast acquisition, thanks to the improvement of the

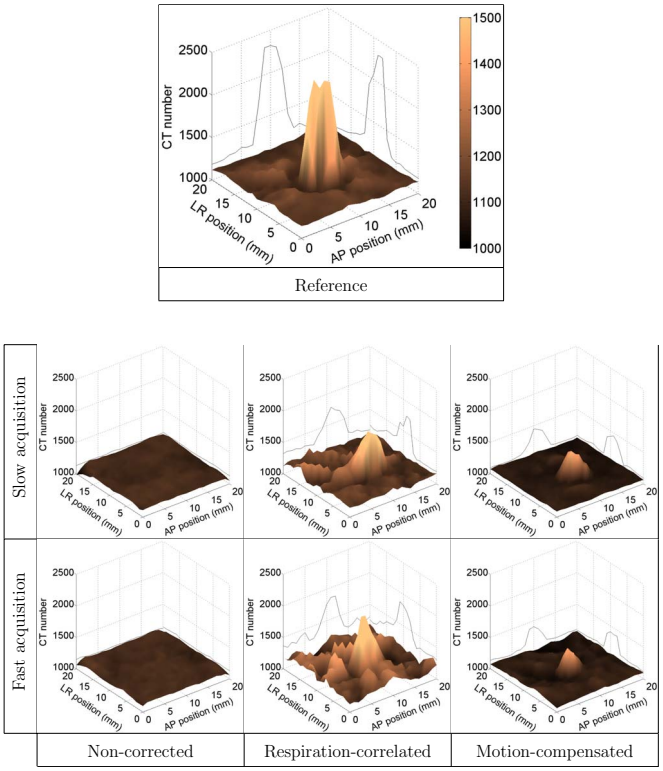

FIG. 8. Surface plot around the marker position of the MIP of 20 axial slices of the CBCT images reconstructed from the three data sets acquired on the mechanical phantom.

angular sampling of the CB projections per respiratory phase. Finally, motion-compensated CBCT corrects for the respiratory motion with reduced noise and streak artifacts.

Figure 8 depicts the marker shape at the center of the ball. The maximum intensity projection (MIP) of 20 axial slices around the marker position was used to make sure that the marker was sampled and not in an adjacent slice due to registration errors. The motion makes the marker invisible in the non-corrected CBCT images. It is distinguishable on the respiration-correlated CBCT images but with noise and streaks in the background. Finally, it is visible on motion-compensated CBCT images with a background noise comparable to the reference CBCT image (stationary phantom).

TABLE II. SNR of the reconstructed CBCT images of the phantom study. The reference CBCT image (stationary phantom) was used as reference.

	Non-corrected	Respiration-correlated	Motion-compensated
Slow acquisition (dB)	7.9	18.5	21.4
Fast acquisition (dB)	7.9	16.3	21.2

Table II gives the SNR values of the reconstructed CBCT images in the ROI and quantitatively confirms the visual observation (Figs. 7 and 8). Low values of non-corrected CBCT images indicate that the motion impacts the expected signal given by the reference image (stationary phantom). Motion correction with respiration-correlated CBCT clearly improves the SNR but a 2.2 dB difference is observed between slow and fast acquisitions. The SNR is further improved with motion-compensated CBCT using both acquisition protocols which indicates that image quality is improved while motion correction is maintained.

III.C. Patient study

Figure 9 shows slices of the MidP and CBCT images of the lung patient after registration. Zooms and profiles of these slices are provided in Fig. 10. The blur induced by the respiratory motion is visible on the non-corrected CBCT images around the tumor and the diaphragm. Like for the phantom results, both respiration-correlated CBCT and motion-compensated CBCT correct for the respiratory induced blur, thus displaying a tumor shape which is closer to the MidP but with less contrast for motion-compensated CBCT im-

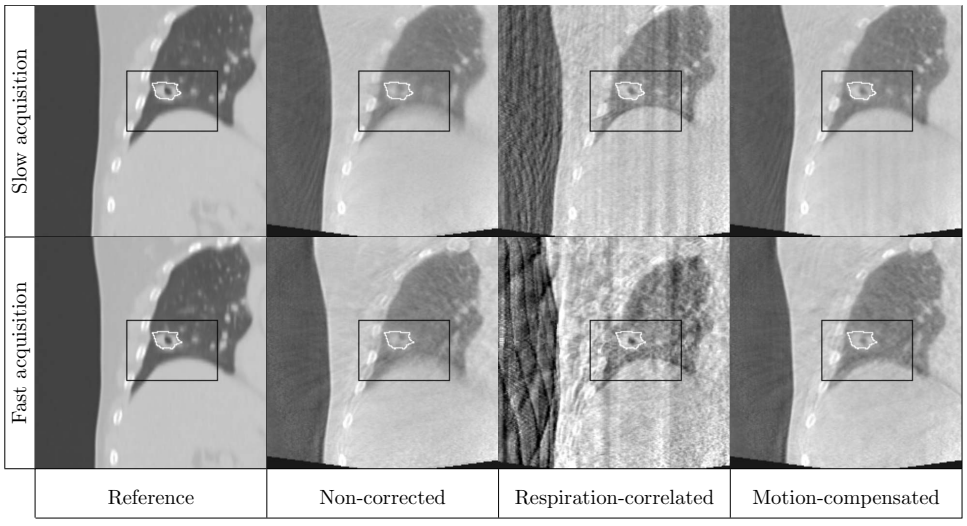

FIG. 9. Coronal slices of the reference CT image and CBCT images reconstructed from the two data sets acquired on the lung patient. The white lines delimit the GTV and the black lines the zooms in Fig. 10. Gray level window: [−500;1500].

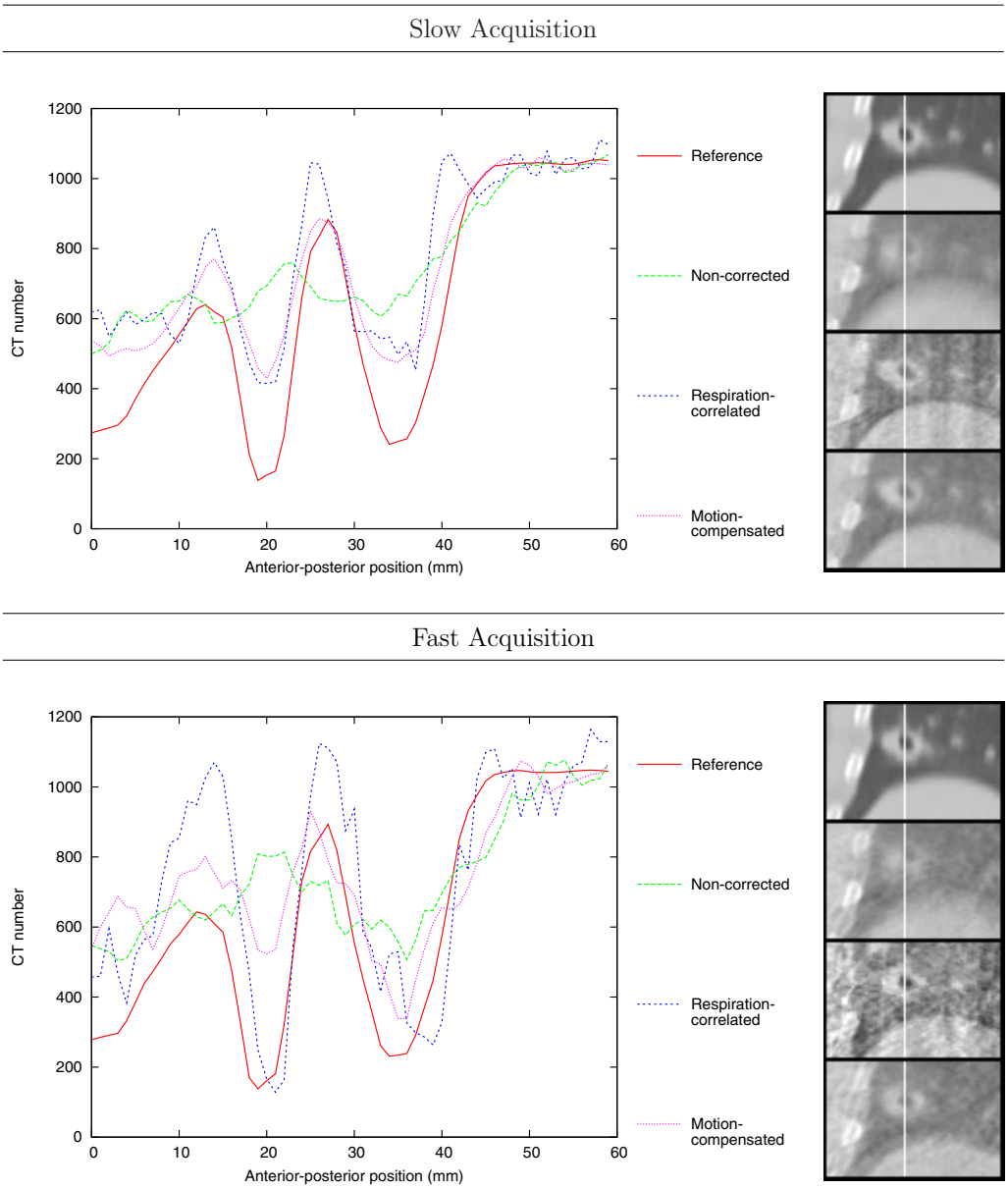

FIG. 10. Left: profiles of the reference CT and CBCT images reconstructed from the slow and fast CB acquisitions of the lung patient. Right: zooms on the coronal slices of the CT images in the regions delimited in Fig. 9 with the white lines corresponding to the profile locations. Gray level window: [−500,1500].

ages. Nevertheless, respiration-correlated CBCT images suffer from noise and streak artifacts characterized by wavelets along the profiles, which is not the case with motion-compensated CBCT images (Fig. 10).

Figure 11 shows slices of the reference CT and CBCT images of the liver patient with two different gray level windows, one for lung visualization and the other for abdominal soft-tissue visualization. The respiratory motion blurs the markers and the bronchial tree in non-corrected CBCT images. These two effects are corrected by respiration-correlated and motion-compensated CBCT but with more pronounced streaks and noise for respiration-correlated CBCT which can hinder the extraction of information in soft-tissue regions. Figure 12 provides surface plots in the rectangle outlined in Fig. 11 which allow to compare the level of background noise. The noise is, in particular, inferior on the motion-compensated CBCT image of the fast acquisition than on the respiration-correlated CBCT image of the slow acquisition.

Table III provides the acquisition time and the reconstruction time of each sequence of patient CB projections. Non-corrected CBCT reconstruction is around three times faster than the acquisition. Respiration-correlated CBCT reconstruction is around 10% slower than non-corrected CBCT reconstruction due to the overhead implied by the estimation of the respiratory signal. Motion-compensated CBCT reconstruction is around two times slower due to warped backprojections but always within the acquisition time. Note that the computational cost of warped backprojections is not constant because it depends on the number of segments used for the warped backprojection (Fig. 3). The number of segments

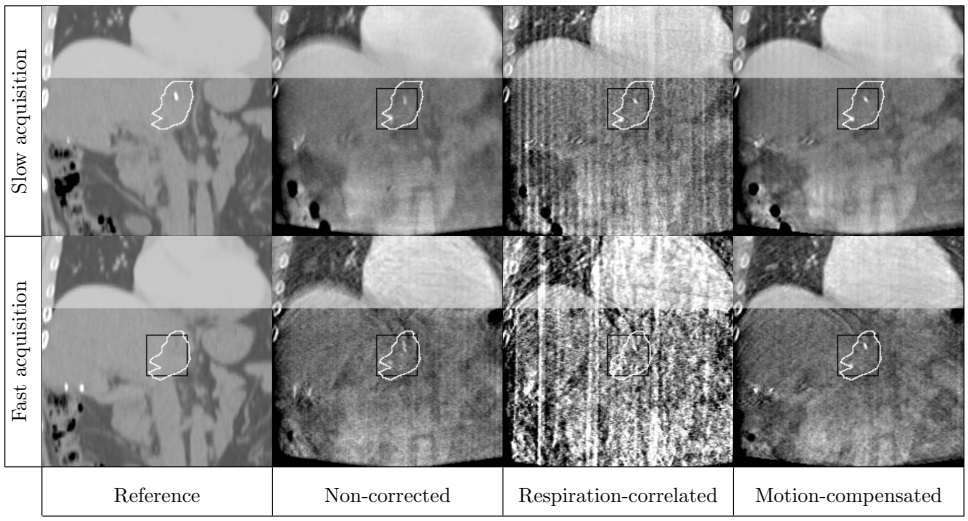

FIG. 11. Coronal slices of the reference CT image and CBCT images reconstructed from the two data sets acquired on the liver patient. The white lines delimit the GTV and the black lines the plot of Fig. 12. Gray level windows: [−500;1500] for the thorax and [600;1300] for the abdomen.

is determined by the criterion [Eq. (4)] which merges segments according to the smoothness of the motion model in the cranio-caudal direction.

IV. DISCUSSION

In this study, we developed an on-the-fly motion-compensated CBCT solution, i.e. estimation and compensation of the respiratory motion in the CBCT reconstruction during the acquisition of the CB projections. Adequate computational efficiency has been obtained by optimizing both the estimation of the respiratory motion and the motion-compensated CBCT reconstruction algorithm.

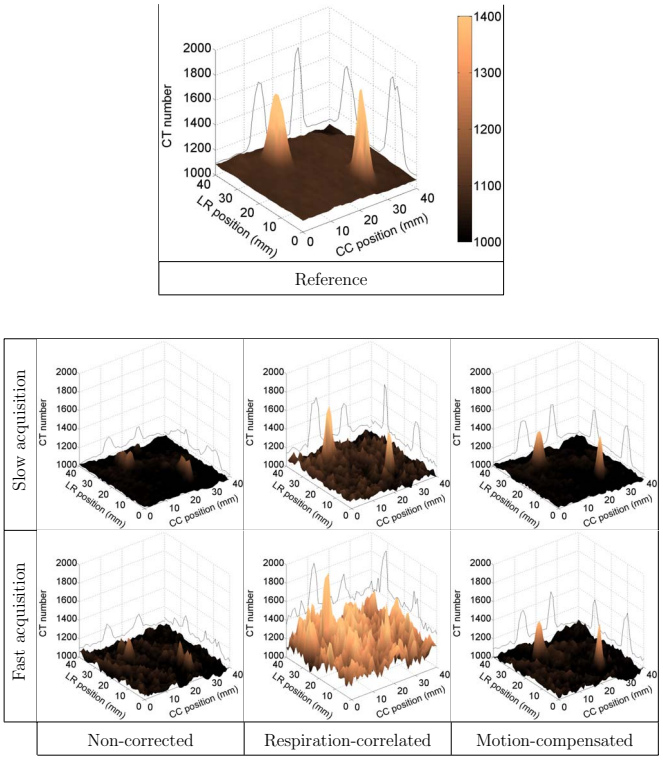

FIG. 12. Surface plot of the MIP of coronal slices in the regions delimited in Fig. 11.

On-the-fly estimation of the respiratory motion was based on an *a priori* model of the patient motion along the respiratory cycle. We assumed that the respiratory motion of each patient is reproducible interfractionally and that it is accurately described by the 4D DVF estimated from the 4D planning CT. Inaccuracies of the 4D DVF due to artifacts of the 4D planning CT (Ref. 15) or misregistration[16] were not specifically evaluated here because the difference between the motion described by the 4D DVF and the actual motion of the patient can always be regarded as a non-reproducibility issue.

The assumption of reproducibility relied on previous studies[17,34] which showed that the respiratory cycle is roughly reproducible, as described by the distribution of the variations of the respiratory cycle observed on interfraction CBCT images (Fig. 6). However, the reproducibility is never perfect so we evaluated the robustness of the method to inaccuracies of the motion estimate. We demonstrated using simulated data that variations of the respiratory cycle affect the image quality proportionally to the motion estimation error (Fig. 6). Consequently, most of the motion is compensated for 90% of the population if the *a priori* model represents the average respiratory cycle. The deviation of the *a priori* model from the mean respiratory cycle will be investigated in future work. Phase shift between the *a priori* motion model and the actual motion is the most sensitive type of motion error. To minimize phase shifts, we evaluated the phase of each frame of the 4D planning CT using the *a priori* motion model [Eq. (3)] and we used an estimate of the respiratory phase of each CB projection based on the respiratory signal extracted from the CB projections. Thus, we process the respiratory phase from the motion of internal structures and exclude phase shifts that could be introduced with the use of an external device.[35,36] Amplitude variations of the

TABLE III. Acquisition and reconstruction times of each CBCT reconstruction method for the phantom and patient data.

Study	Gantry speed	Acquisition time (s)	Reconstruction time (s)		
			Non-corrected	Respiration-correlated (all ten frames)	Motion-compensated
Lung patient	Slow	254	90	99	199
	Fast	66	24	25	61
Liver patient	Slow	241	78	88	151
	Fast	40	13	15	39

respiratory motion are less sensitive because the motion is still corrected in the right direction even if not to the exact extent. Finally, setup errors are very insensitive because the motion is spatially smooth in the lungs which implies that using the motion of a neighboring voxel instead of the actual motion of the voxel has a limited impact. The same is true for baseline shifts which have locally the same effect as setup errors. Nevertheless, the motion is not smooth everywhere, e.g. along the thoracic walls due to the so-called sliding effect,[19] and great care should be observed for these anatomical sites. If a large setup error is estimated from the CBCT image after reconstruction based on bony anatomy[31] and such an anatomical site of interest, the motion-compensated CBCT image can be reconstructed again with the setup error corrected in the spatial positioning of the motion model.

The reconstruction algorithm was based on the FDK algorithm as proposed by Li *et al.*[9] The respiratory motion was compensated for by warping each backprojection depending on the respiratory motion (Fig. 2). The method is heuristic and the local correction is not perfect even if the motion estimation is perfect:[33] respiration-induced blur is removed but streaks are not corrected in static parts and might be emphasized in moving parts (Fig. 5). The remaining artifacts can explain that small changes of the motion model are not captured by our evaluation metric (Fig. 6). To our knowledge, only iterative reconstruction has shown better compensation for such motion[33] but such algorithms are not applicable for on-the-fly reconstruction.

Backprojection is the most time-consuming step of FDK algorithm. In non-corrected CBCT, the key points of the optimization are the use of the preservation of the straightness with the x-ray projection transform to minimize the computational operations and the reordering in memory of image data to optimize the cache memory flow.[29,37] Warping the backprojection potentially eliminates these two optimizations. However, we proposed to split the warped CT image in piecewise linear segments based on two user parameters l and m which respectively represent the minimal length of the segment pieces and a threshold for merging them based on the actual motion of the respiratory cycle (Fig. 3). Although not as efficient as the inner loop of the non-corrected case, an optimized loop can then be used along each segment, which minimizes the computational loss compared to non-corrected CBCT. The effect on image quality of the underlying approximations is negligible (Figs. 4 and 5). Moreover, memory cache flow is not significantly affected because the voxels of the CBCT image are still covered in their sequential order in memory and because the respiratory motion is mostly cranio-caudal, which is also the direction of the sequential order in memory of the pixels of the CB projections. Currently, the backprojection speed is limited by a different factor depending on the method: warped backprojection is mostly limited by computation cost, contrarily to straight backprojection which is mostly limited by cache memory flow. As a consequence, the speed gap between straight and warped backprojection might increase or decrease depending on future hardware evolutions.

The image quality of motion-compensated CBCT images was compared to non-corrected and respiration-correlated CBCT images on slow and fast acquisitions of a mechanical phantom (Figs. 7 and 8), a lung patient (Figs. 9 and 10), and a liver patient (Figs. 11 and 12). Non-corrected CBCT images contain artifacts caused by the motion, mainly smoothing of tissue boundaries, which are clearly visible when compared to the reference CT image. Respiration-correlated CBCT corrects for the motion but the use of a subset of the CB projections to reconstruct a phase of the respiratory cycle implies streak artifacts (Figs. 9 and 11) caused by view aliasing.[6,7] Improving image quality of respiration-correlated CBCT requires a better angular sampling of the CB projections per respiratory phase which was obtained in our current acquisition protocol by slowing down the rotation speed of the gantry from 200°/min to 50°/min. Even so, soft-tissue visualization is still challenging in the upper abdomen (Fig. 11). Finally, motion-compensated CBCT corrects for the respiratory motion without view-aliasing artifacts because all the CB projections are used for the reconstruction of a single 3D CBCT image. Tissue boundaries are recovered (Figs. 7 and 10) and fine structures such as markers are visible even with a fast acquisition (Figs. 8 and 12). Background noise of the motion-compensated CBCT images reconstructed from the fast acquisition is inferior or equal to the one of the respiration-correlated CBCT images reconstructed from the slow acquisition (Figs. 8, 10, and 12). The contrast-to-noise ratio is then acceptable for extraction of soft-tissue information in the upper abdomen.

The design of the method was driven by clinical needs. Although respiration-correlated CBCT has been successfully implemented clinically in our hospital, adequate image quality required an acquisition time of 4 min instead of 1 min for static CBCT, which lengthens the fraction duration (and in-

creases the patient dose if the x-ray tube parameters are not modified). On the contrary, our results indicate that motion-compensated CBCT does not require a modification of the acquisition protocol compared to static CBCT. Improvement of image quality should also allow better visualization of smaller and/or less contrasted tumors, for example, mediastinal targets. Besides, the method was designed to keep an essential feature of respiration-correlated CBCT for adaptive radiation therapy (ART):[2] the anatomical changes of the patient between the planning CT and the CBCT acquisitions are still visible as only a cyclic motion is compensated for during reconstruction (Sec. II C). Moreover, the reconstruction process ends within a few seconds after the end of the acquisition (Table III) which is required to adapt the treatment during the treatment fractions (online ART).

One of the common concerns for clinical application of methods using non-rigid registration is the accuracy of the motion estimation and the consequences of inaccuracies. We addressed this issue by forcing the estimated motion to be null on average over the CB acquisition (Sec. II C). If the motion is not accurately estimated, the fact that it is null on average implies only residual blur around the mean position over the CB acquisition and prevents apparent but inaccurate shifts. The same is not true for methods which warp an *a priori* CT image using the estimated motion.[38–40] Irregularity of the respiratory motion during the CB acquisition will also imply residual blur as is the case with respiration-correlated CBCT.[7] Note that using the end-exhale frame in our evaluation probably minimized the impact of irregularities on the respiration-correlated CBCT images because it is generally the most reproducible phase of the respiratory cycle.[7] Finally, refinement of the estimated motion is possible using more advanced methods[11,41,42] but a first study on 26 CBCT images of three patients has shown promising results[43] and refinement does not seem required for the clinical application of the method.

V. CONCLUSION

We developed a method to estimate the respiratory motion and compensate for it in the reconstruction during the CB acquisition. Results obtained from simulation, phantom, and patient data sets show that the method corrects most of the motion artifacts even without modification of the acquisition protocol used for static CBCT. Moreover, it is fast enough to allow on-the-fly reconstruction within the acquisition time. The method is therefore a solution for correcting the respiratory motion which could advantageously replace respiration-correlated CBCT. It will be implemented clinically in our hospital after validation on a larger set of patients.

[a]Author to whom correspondence should be addressed. Electronic mail: j.sonke@nki.nl

[1]D. Jaffray, J. Siewerdsen, J. Wong, and A. Martinez, "Flat-panel cone-beam computed tomography for image-guided radiation therapy," Int. J. Radiat. Oncol., Biol., Phys. **53**, 1337–1349 (2002).
[2]D. Yan, F. Vicini, J. Wong, and A. Martinez, "Adaptive radiation therapy," Phys. Med. Biol. **42**, 123–132 (1997).
[3]P. Keall, G. Mageras, J. Balter, R. Emery, K. Forster, S. Jiang, J. Kapatoes, D. Low, M. Murphy, B. Murray, C. Ramsey, M. van Herk, S. Vedam, J. Wong, and E. Yorke, "The management of respiratory motion in radiation oncology report of AAPM Task Group 76," Med. Phys. **33**, 3874–3900 (2006).
[4]L. Dietrich, S. Jetter, T. Tücking, S. Nill, and U. Oelfke, "Linac-integrated 4D cone beam CT: First experimental results," Phys. Med. Biol. **51**, 2939–2952 (2006).
[5]S. Kriminski, M. Mitschke, S. Sorensen, N. Wink, P. Chow, S. Tenn, and T. Solberg, "Respiratory correlated cone-beam computed tomography on an isocentric C-arm," Phys. Med. Biol. **50**, 5263–5280 (2005).
[6]T. Li, L. Xing, P. Munro, C. McGuinness, M. Chao, Y. Yang, B. Loo, and A. Koong, "Four-dimensional cone-beam computed tomography using an on-board imager," Med. Phys. **33**, 3825–3833 (2006).
[7]J.-J. Sonke, L. Zijp, P. Remeijer, and M. van Herk, "Respiratory correlated cone beam CT," Med. Phys. **32**, 1176–1186 (2005).
[8]M. van Herk, L. Zijp, P. Remeijer, J. Wolthaus, and J.-J. Sonke, *International Conference on the Use of Computers in Radiation Therapy (ICCR)* (Novel Digital, Toronto, 2007), pp. 33–37.
[9]T. Li, E. Schreibmann, Y. Yang, and L. Xing, "Motion correction for improved target localization with on-board cone-beam computed tomography," Phys. Med. Biol. **51**, 253–267 (2006).
[10]T. Li, A. Koong, and L. Xing, "Enhanced 4D cone-beam CT with inter-phase motion model," Med. Phys. **34**, 3688–3695 (2007).
[11]R. Zeng, J. Fessler, and J. Balter, "Estimating 3-D respiratory motion from orbiting views by tomographic image registration," IEEE Trans. Med. Imaging **26**, 153–163 (2007).
[12]J. Wolthaus, C. Schneider, J.-J. Sonke, M. van Herk, J. Belderbos, M. Rossi, J. Lebesque, and E. Damen, "Mid-ventilation CT scan construction from four-dimensional respiration-correlated CT scans for radiotherapy planning of lung cancer patients," Int. J. Radiat. Oncol., Biol., Phys. **65**, 1560–1571 (2006).
[13]M. Hemmendorff, M. Andersson, T. Kronander, and H. Knutsson, "Phase-based multidimensional volume registration," IEEE Trans. Med. Imaging **21**, 1536–1543 (2002).
[14]J. Wolthaus, J.-J. Sonke, M. van Herk, and E. Damen, "Reconstruction of a time-averaged midposition CT scan for radiotherapy planning of lung cancer patients using deformable registration," Med. Phys. **35**, 3998–4011 (2008).
[15]T. Yamamoto, U. Langner, B. Loo, J. Shen, and P. Keall, "Retrospective analysis of artifacts in four-dimensional CT images of 50 abdominal and thoracic radiotherapy patients," Int. J. Radiat. Oncol., Biol., Phys. **72**, 1250–1258 (2008).
[16]R. Kashani, M. Hub, J. Balter, M. Kessler, L. Dong, L. Zhang, L. Xing, Y. Xie, D. Hawkes, J. Schnabel, J. McClelland, S. Joshi, Q. Chen, and W. Lu, "Objective assessment of deformable image registration in radiotherapy: A multi-institution study," Med. Phys. **35**, 5944–5953 (2008).
[17]J.-J. Sonke, J. Lebesque, and M. van Herk, "Variability of four-dimensional computed tomography patient models," Int. J. Radiat. Oncol., Biol., Phys. **70**, 590–598 (2008).
[18]H. Shirato, Y. Seppenwoolde, K. Kitamura, R. Onimura, and S. Shimizu, "Intrafractional tumor motion: lung and liver," Semin. Radiat. Oncol. **14**, 10–18 (2004).
[19]Z. Wu, E. Rietzel, V. Boldea, D. Sarrut, and G. Sharp, "Evaluation of deformable registration of patient lung 4DCT with subanatomical region segmentations," Med. Phys. **35**, 775–781 (2008).
[20]L. Zijp, J.-J. Sonke, and M. van Herk, *International Conference on the Use of Computers in Radiation Therapy (ICCR)* (Jeong, Seoul, Republic of Korea, 2004), pp. 507–509.
[21]P. Keall, G. Starkschall, H. Shukla, K. Forster, V. Ortiz, C. Stevens, S. Vedam, R. George, T. Guerrero, and R. Mohan, "Acquiring 4D thoracic CT scans using a multislice helical method," Phys. Med. Biol. **49**, 2053–2067 (2004).
[22]T. Pan, T. Lee, E. Rietzel, and G. Chen, "4D-CT imaging of a volume influenced by respiratory motion on multi-slice CT," Med. Phys. **31**, 333–341 (2004).
[23]L. Feldkamp, L. Davis, and J. Kress, "Practical cone-beam algorithm," J. Opt. Soc. Am. A **1**, 612–619 (1984).
[24]N. Mail, P. O'Brien, and G. Pang, "Lag correction model and ghosting analysis for an indirect-conversion flat-panel imager," J. Appl. Clin. Med. Phys. **8**, 2483 (2007).
[25]R. Boellaard, M. van Herk, H. Uiterwaal, and B. Mijnheer, "Two-dimensional exit dosimetry using a liquid-filled electronic portal imaging device and a convolution model," Radiother. Oncol. **44**, 149–157 (1997).

[26]D. Parker, "Optimal short scan convolution reconstruction for fanbeam CT," Med. Phys. **9**, 254–257 (1982).
[27]B. Ohnesorge, T. Flohr, K. Schwarz, J. Heiken, and K. Bae, "Efficient correction for CT image artifacts caused by objects extending outside the scan field of view," Med. Phys. **27**, 39–46 (2000).
[28]M. van Herk, A. Betgen, B. Brand, D. Jaffray, P. Remeijer, M. Smitsmans, J.-J. Sonke, and L. Zijp, *International Conference on the Use of Computers in Radiation Therapy (ICCR)* (Jeong, Seoul, Republic of Korea, 2004), pp. 504–506.
[29]M. Kachelrieß, M. Knaup, and O. Bockenbach, "Hyperfast parallel-beam and cone-beam backprojection using the cell general purpose hardware," Med. Phys. **34**, 1474–1486 (2007).
[30]P. Joseph, "An improved algorithm for reprojecting rays through pixel images," IEEE Trans. Med. Imaging **1**, 192–196 (1982).
[31]G. Borst, J.-J. Sonke, A. Betgen, P. Remeijer, M. van Herk, and J. Lebesque, "Kilo-voltage cone-beam computed tomography setup measurements for lung cancer patients: First clinical results and comparison with electronic portal-imaging device," Int. J. Radiat. Oncol., Biol., Phys. **68**, 555–561 (2007).
[32]R. Louwe, M. Wendling, M. van Herk, and B. Mijnheer, "Three-dimensional heart dose reconstruction to estimate normal tissue complication probability after breast irradiation using portal dosimetry," Med. Phys. **34**, 1354–1363 (2007).
[33]S. Rit, D. Sarrut, and L. Desbat, "Comparison of analytic and algebraic methods for motion-compensated cone-beam CT reconstruction of the thorax," IEEE Trans. Med. Imaging (in press).
[34]D. Michalski, M. Sontag, F. Li, R. de Andrade, I. Uslene, E. Brandner, D. Heron, N. Yue, and M. Huq, "Four-dimensional computed tomography-based interfractional reproducibility study of lung tumor intrafractional motion," Int. J. Radiat. Oncol., Biol., Phys. **71**, 714–724 (2008).
[35]J. Killoran, A. Allen, B. Kann, and Y. Lyatskaya, "Inter fractional variability of breathing phase definition as determined by fiducial location," Med. Phys. **35**, 753–763 (2008).
[36]H. Yan, F.-F. Yin, G.-P. Zhu, M. Ajlouni, and J. Kim, "The correlation evaluation of a tumor tracking system using multiple external markers," Med. Phys. **33**, 4073–4084 (2006).
[37]C. Riddell and Y. Trousset, "Rectification for cone-beam projection and backprojection," IEEE Trans. Med. Imaging **25**, 950–962 (2006).
[38]C. Badea, E. Schreibmann, and T. Fox, "A registration based approach for 4D cardiac micro-CT using combined prospective and retrospective gating," Med. Phys. **35**, 1170–1179 (2008).
[39]J. Ehrhardt, R. Werner, D. Säring, T. Frenzel, W. Lu, D. Low, and H. Handels, "An optical flow based method for improved reconstruction of 4D CT data sets acquired during free breathing," Med. Phys. **34**, 711–721 (2007).
[40]L. Ren, J. Zhang, D. Thongphiew, D. Godfrey, Q. Wu, S.-M. Zhou, and F.-F. Yin, "A novel digital tomosynthesis (DTS) reconstruction method using a deformation field map," Med. Phys. **35**, 3110–3115 (2008).
[41]T. Li and L. Xing, "Optimizing 4D cone-beam CT acquisition protocol for external beam radiotherapy," Int. J. Radiat. Oncol., Biol., Phys. **67**, 1211–1219 (2007).
[42]J. Vandemeulebroucke, P. Clarysse, J. Kybic, and D. Sarrut, Proceedings of the First International Workshop on Pulmonary Image Analysis, September 6, 2008 in New York as part of the MICCAI Workshop program, pp. 83–92.
[43]S. Rit, J. Wolthaus, M. van Herk, and J.-J. Sonke, *Medical Image Computing and Computer-Assisted Intervention* (MICCAI, New York, 2008), Vol. 5241, pp. 729–736.